Photocatalytic hydrogen production over Aurivillius compound Bi$_3$TiNbO$_9$ and its modifications by Cr/Nb co-doping

Lu Jiang[a], Shuang Ni[b], Gang Liu[c], Xiaoxiang Xu[a,*]

[a] Shanghai Key Lab of Chemical Assessment and Sustainability, School of Chemical Science and Engineering, Tongji University, 1239 Siping Road, Shanghai, 200092, China
[b] Science and Technology on Plasma Physics Laboratory, Laser Fusion Research Center, China Academy of Engineering Physics, Mianyang 621900, China
[c] Shenyang National laboratory for Materials Science, Institute of Metal Research, Chinese Academy of Science, 72 Wenhua Road, Shenyang 110016, China

A B S T R A C T

In this work, we have applied Cr/Nb co-doping strategy to the wide band gap semiconductor Bi$_3$TiNbO$_9$ and have performed a detailed investigation on the structure, optical and photocatalytic properties of these modified Aurivillius compounds Bi$_3$Ti$_{1-2x}$Cr$_x$Nb$_{1+x}$O$_9$ (x = 0, 0.1, 0.2, 0.3). Our results suggest that Cr/Nb doping slightly expand the unit cell of Bi$_3$TiNbO$_9$ with a doping limit around 20%. The involvement of Cr/Nb dopants in the crystal structure significantly reduces the band gap of Bi$_3$TiNbO$_9$ by nearly 1 eV. Photocatalytic experiments and photoelectrochemical measurements confirms the critical role of Cr/Nb dopants in improving photocatalytic hydrogen production and anodic photocurrent. More than two-fold enhancement in hydrogen production has been noticed for merely 10% Cr/Nb co-doping. The highest photocatalytic activity belongs to Bi$_3$Ti$_{0.8}$Cr$_{0.1}$Nb$_{1.1}$O$_9$ (x = 0.1) for full range illumination and to Bi$_3$Ti$_{0.6}$Cr$_{0.2}$Nb$_{1.2}$O$_9$ (x = 0.2) for visible light illumination, with apparent quantum efficiency (AQE) approaching 0.52% and 0.27%, respectively. DFT calculation discloses the role of Cr in forming a new valence band inside the band gap of Bi$_3$TiNbO$_9$. In addition, strong anisotropic phenomenon in charge transportation of Bi$_3$TiNbO$_9$ is also verified by DFT, as both conduction band minimum (CBM) and valence band maximum (VBM) are buried in the [BiTiNbO$_7$]$^{2-}$ perovskite slabs and charges are only allowed to migrate within the slabs.

© 2017 Elsevier B.V. All rights reserved.

1. Introduction

Fossil fuel shortage and environmental issues associated with fossil fuel usage have been an on-going threat to the sustainability of our modern society [1,2]. There has been an increasing agreement on searching clean and renewable energy resources and/or developing green energy technologies that can significantly relieve us from fossil fuel reliance [3,4]. Water splitting into H$_2$ and O$_2$, driven by semiconductor photocatalysts under solar insolation, offers a promising scenario towards establishing a clean and sustainable energy infrastructure that can decarbonize our fossil fuel-based economy [5–12]. The practical deployment of this tempting technique essentially depends on the significant advances in photocatalysts where breakthrough on solar to hydrogen efficiency (STH) can be achieved [13,14]. The low STH of current photocatalysts stems largely from their large band gaps that allow

absorption exclusively to UV photons, accounting for merely 4% of entire solar spectrum [15]. Thereby, band gap management is taken as the premier target for developing efficient photocatalysts. For instance, reducing the band gap value from 3.2 eV to 2.0 eV enormously increases the theoretical STH from less than 1% to almost 16% [15]. Apart from poor light absorption, current photocatalysts also suffers from rapid charge recombination events, being another major obstacle for realizing high STH [16]. Recent studies have witnessed a number of efficient perovskite photocatalysts with layered crystal structures, albeit most of them are wide band gap semiconductors e.g. Sr$_2$Nb$_2$O$_7$ [17], Ba$_5$Nb$_4$O$_{15}$ [18], K$_2$La$_2$Ti$_3$O$_{10}$ [19], etc. There seems a strong correlation between structural lamination and charge separation among these compounds [20–23]. Thereby, layered perovskites with visible light absorption are of particular interest. In this regard, Aurivillius compounds have gained considerable attention due to their peculiar laminated crystal structures and desirable visible light sensitivity, e.g. Bi$_2$WO$_6$ [24–26], Bi$_4$Ti$_3$O$_{12}$ [27–29] etc. Their chemical formula can be written as (Bi$_2$O$_2$)[A$_{m-1}$B$_m$O$_{3m+1}$] (m ≥ 1) where Bi$_2$O$_2$ in the parenthesis denotes the layers with fluorite-like structure

and $A_{m-1}B_mO_{3m+1}$ in the square bracket represents the slabs of perovskite-type architecture [30]. The crystal structure of Aurivillius compounds can then be described as alternatively stacking of Bi_2O_2 layers and $A_{m-1}B_mO_{3m+1}$ slabs along perovskite $[001]_p$ direction. Many Aurivillius compounds are ferroelectrics whose spontaneous polarization (Ps) is extremely useful for separation of photo-generated electron-hole pairs. For instance, $Bi_4Ti_3O_{12}$ single crystals have Ps of 4 μC cm^{-2} along c-axis [31], which is responsible for its superior photocatalytic activity observed as charge recombination events in this compound is effectively reduced [28]. More importantly, the involvement of perovskite slabs in the Aurivillius compounds enables various compositional and structural modifications feasible. For example, by simple doping Cr into $Bi_4Ti_3O_{12}$, strong visible light absorption as far as 600 nm and efficient hydrogen production from water under visible light illumination can be realized [27,29]. In this work, we performed a systematic investigation on Aurivillius compound Bi_3TiNbO_9 and its Cr/Nb co-doped counterparts for photocatalytic hydrogen production from water. Bi_3TiNbO_9 has almost the highest Curie temperature (T_c) ~914 °C among ceramics known to date therefore can maintain its ferroelectric properties over a wide temperature range [32–35]. Previous studies on pristine Bi_3TiNbO_9 suggest promising photocatalytic activities in dye degradation under UV or visible light illumination [36,37], yet photocatalytic hydrogen production from water, which is more intriguing from energy conversion point of view, has not been investigated for this compound. Our study indicates that Bi_3TiNbO_9 is a UV light sensitive photocatalyst for hydrogen production from water and can be tuned into visible light active one upon Cr/Nb co-doping.

2. Experimental

2.1. Materials synthesis

Bi_3TiNbO_9 and its Cr/Nb co-doped ones $Bi_3Ti_{1-2x}Cr_xNb_{1+x}O_9$ (x = 0.1, 0.2, 0.3) were prepared by solid state reactions: calculated amounts of Bi_2O_3 (Aladdin, 99.9%), rutile TiO_2 (Aladdin, 99.99%), Nb_2O_5 (Aladdin, 99.99%) and Cr_2O_3 (Aladdin, 99%) were mixed by using an agate mortar and pestle. Raw powders were pretreated in a muffle furnace at 300 °C for 3 h prior to weighing for the purpose to eliminate moisture absorbed. The admixtures of these powders were then uniaxially pressed into pellets under a pressure of 5 tons and were transferred into alumina crucibles for further calcination. The typical calcining temperature is 850 °C and duration time of 24 h. Intermediate grindings and re-calcination were applied for the removal of secondary phases. The calcined pellets were finally ground into powders and collected for further analysis. Cr doped sample was also prepared for comparison purpose without adding Nb_2O_5 in the initial step.

2.2. Materials characterization

Phase identification and crystal structure were performed using X-ray powder diffraction (XRD) techniques on a Bruker D8 Focus diffractometer. Incident X-ray radiation is Cu $K_{\alpha1}$ (λ = 1.5406 Å) and Cu $K_{\alpha2}$ (λ = 1.5444 Å). Typical step size and collection time is 0.01° and 0.1s. Rietveld refinement was carried out on XRD data using General Structure Analysis System (GSAS) software package [38]. Microstructures of freshly prepared samples were examined by a field emission scanning electron microscope (Hitachi S4800) and a transmission electron microscope (JEOL JEM-2100). Optical absorption data were collected on a UV–vis spectrophotometer coupled with integrating sphere (JASCO-750) and data were analyzed using JASCO software suite. $BaSO_4$ was used as a reference non-absorbing material [39]. Surface conditions were analyzed by X-ray photo-

electron spectroscopy (Thermo Escalab 250 with a monochromatic Al Kα X-ray source). All bonding energies were adjusted according to adventitious carbon C 1s peak at 284.7 eV [40]. The surface area of as-prepared samples was analyzed on a Micro-meritics instrument TriStar 3000 and were calculated based on the Brunauer-Emmett-Teller (BET) model.

2.3. Photocatalytic activity

Photocatalytic hydrogen production experiments were carried out in a top-irradiation-type reactor connected to a gas-closed circulation and evacuation system (Perfect Light, Labsolar-IIIAG). In a typical experiment, 100 mg sample powders were ultrasonically dispersed into 100 ml Na_2SO_3 aqueous solution (0.05 M) .The whole suspension was then sealed in the reactor and evacuated in order to remove dissolved air. Photocatalytic experiment was initiated by irradiating the suspension with UV or visible light and gas composition within the reactor was monitored by an on-line gas chromatograph (TECHCOMP, GC7900) with a TCD detector (5 Å molecular sieve columns and Ar carrier gas). The temperature of the reactor was maintained at 293 K by applying a water jacket. Here, Na_2SO_3 aqueous solution serves as a sacrificial agent to promote photo-reduction reactions. 1 wt% Pt was loaded onto sample powders as a co-catalyst according to previous reports [41–45]: proper amounts of H_2PtCl_6 aqueous solution was impregnated into sample powders and was dried on a hot-plate at 90 °C. The temperature of the hot-plate was then raised to 180 °C for 2 h to convert H_2PtCl_6 into Pt nanoparticles. Light source in these experiments is a 500 W high-pressure mercury lamp (NbeT, Merc-500). Visible light illumination was generated by filtering the lamp output with a UV cutoff filter (λ ≥ 420 nm). The photon flux of the lamp is calibrated using a quantum meter (Apogee MP-300). The recorded photon flux is ~1543.9 μmol/m^2/s for full range irradiation (λ ≥ 250 nm) and ~668.5 μmol/m^2/s for visible light irradiation (λ ≥ 420 nm). Photons at a particular wavelength (i.e. 420 nm) was generated by filtering the output of a Xenon lamp (Perfect Light, PLX-SXE300) with a band pass filter (λ = 420 nm). The recorded photon flux is 228.56 μmol/m^2/s. The apparent quantum efficiency (AQE) is then calculated using the following equation:

Apparent quantum efficiency = 2 × mol of hydrogen production

per hour/moles of photon flux per hour × 100%

2.4. Photoelectrochemical measurements

Photoelectrodes were fabricated by an electrophoretic deposition method [46–49]: two pieces of clean fluorine doped tin oxide (FTO) glass (30 × 10 mm) were immersed inside 50 ml acetone solution containing 40 mg ultrasonically dispersed sample powders and 10 mg iodine. The two pieces of glass were aligned in parallel with 10 mm distance with conductive part faced inward. Subsequently, they were subjected to a constant electrical bias (10 V) under potentiostatic control (Keithley 2450 Source meter) for 3 min. The as-prepared photoelectrodes were fired at 473 K for 10 min for the removal of iodine absorbed. Diluted $TiCl_4$ (Alfa-Aesar, 99.9%) methanol solution (10 mM) was dropped onto the electrodes and was dried in air. The procedure was repeated six times in order to minimize the exposure of naked FTO. The electrodes were then calcined at 673 K for 1 h to strengthen the particle contact. Photoelectrochemical measurements were carried out in a three-electrode configuration under the control of a Zahner electrochemical workstation. The as-prepared electrode, Pt foil (10 × 10 mm) and Ag/AgCl electrode were used as the working, counter and reference electrodes, respectively. An aqueous solu-

tion of K_3PO_4/K_2HPO_4 (0.1 M, pH = 7.95) was used as an electrolyte and a buffer. A 300 W Xenon lamp (Perfect Light, PLX-SXE300) coupled with a UV cutoff filter ($\lambda \geq 420$ nm) or AM1.5 filter was applied as the light source. The incident light was rectified by an electronic timer and shutter (DAHENG, GCI-73).

2.5. Theoretical calculations

Density functional theory implemented in the Vienna Ab initio Simulation Package (VASP) was used to perform theoretical calculations [50]. Here, the Perdew, Burke and Ernzerhof (PBE) exchange-correlation functional within the generalized gradient approxiamtion (GGA) were used [51] and the projector augmented-wave pseudopotential were applied [52]. An orthorhombic unit cell ($a = 5.44$ Å, $b = 5.42$ Å, $c = 25.14$ Å, $\alpha = \beta = \gamma = 90°$) was configured for Bi_3TiNbO_9 simulations (56 atoms in total). Atomic positions were taken according to Rietveld refinement results. Cr/Nb co-doping was considered simply by replacing 2 Ti atoms with 1 Cr and 1 Nb. All geometry structures were fully relaxed until forces on each atom are less than 0.01 eV/ Å. Static calculations were performed with a $10 \times 10 \times 3$ Monkhorst-Pack k-point grid [53].

3. Results and discussions

3.1. Phase identification and crystal structure

Phase compositions of as-prepared samples were first analyzed using X-ray powder diffraction (XRD) techniques. Fig. 1 illustrates the XRD patterns of $Bi_3Ti_{1-2x}Cr_xNb_{1+x}O_9$ (x = 0, 0.1, 0.2, 0.3). Sharp peaks similar to standard Bi_3TiNbO_9 (x = 0) patterns (JCPDS 01-079-1550) can be identified up to x = 0.2, indicating the formation of single phase. These peaks can be well indexed using an orthorhombic symmetry, suggesting that the crystal structure of Aurivillius compound Bi_3TiNbO_9 is maintained after Cr/Nb co-doping. The doping limit or the maximal dissolution of Cr/Nb in Bi_3TiNbO_9 lies probably close to 20% as further increasing x to 0.3 leads to the formation of a secondary phase $Bi_{1.34}CrNbO_6$, presumably due to the excessive Cr and Nb. We then carried out Rietveld refinement on the diffraction data based on structure information of
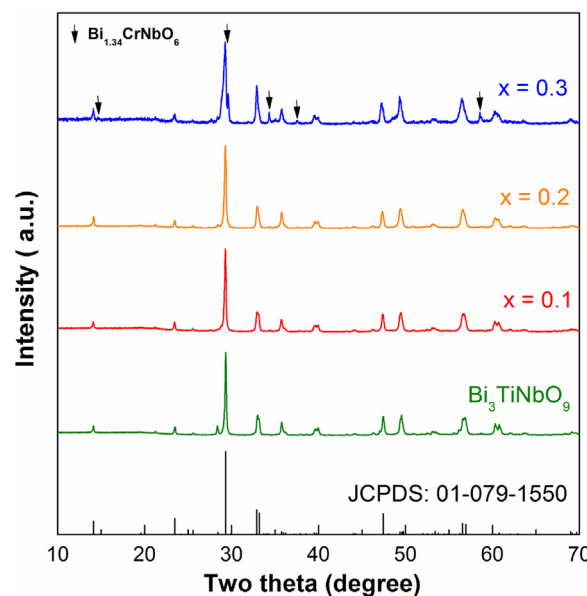
Fig. 1. X-ray powder diffraction patterns of freshly prepared sample $Bi_3Ti_{1-2x}Cr_xNb_{1+x}O_9$ (x = 0, 0.1, 0.2, 0.3). Vertical bars of standard Bi_3TiNbO_9 (x = 0) patterns (JCPDS 01-079-1550) are shown at the bottom. Impurity peaks corresponding to $Bi_{1.34}CrNbO_6$ are labelled by arrows (↓).

pristine Bi_3TiNbO_9. Reasonable goodness-of-fit parameters (R_p, R_{wp} and χ^2) were only achieved by introducing the constraints that Ti, Nb and Cr were accommodated in the same crystallographic position. Typical refinement results for $Bi_3Ti_{0.6}Cr_{0.2}Nb_{1.2}O_9$ (x = 0.2) is displayed in Fig. 2 and all refined unit cell parameters are tabulated in Table 1. It is clear from Table 1 that introducing Cr/Nb induces expansion of unit cell, which can be explained by the substitution of small Ti^{4+} cation with large Cr^{3+}/Nb^{5+} cations according to Vegard's law (ionic radius in octahedral coordination: $r_{Ti4+} = 0.605$ Å, $r_{Cr3+} = 0.615$ Å and $r_{Nb5+} = 0.64$ Å [54,55]). The replacement of Ti with Cr/Nb is likely to be random as super-lattice peaks due to cation ordering are not discernable in all diffraction patterns. The crystal structure of Cr/Nb co-doped Bi_3TiNbO_9 can be viewed as dis-
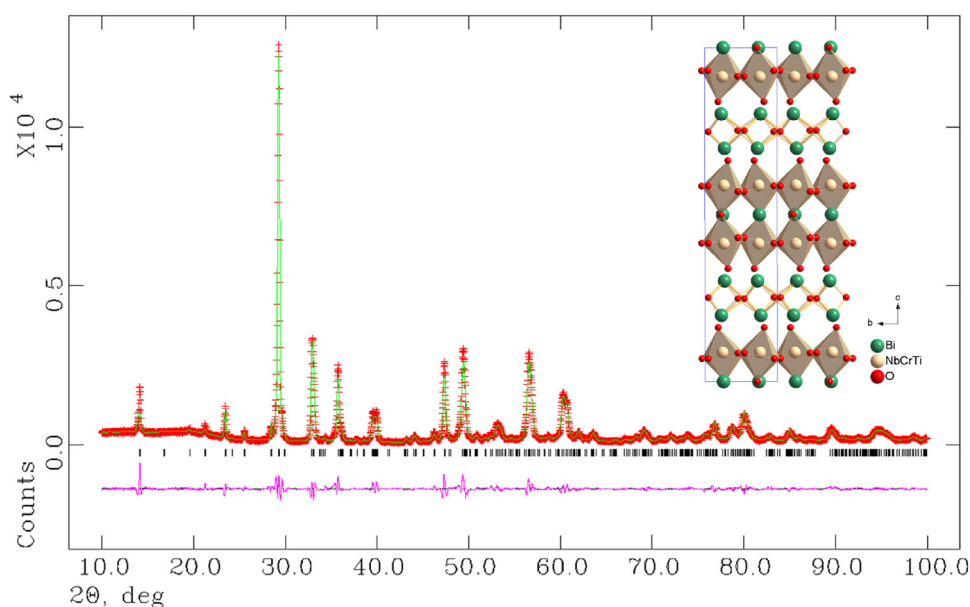
Fig. 2. Observed and calculated X-ray powder diffraction patterns for sample $Bi_3Ti_{0.6}Cr_{0.2}Nb_{1.2}O_9$ (x = 0.2). The refinements converged with good R-factors (R_p = 11.63%, R_{wp} = 8.55%, χ^2 = 4.937). Schematic representation of refined crystal structure is shown as inserted image, unit cell is marked by blue lines. (For interpretation of the references to colour in this figure legend, the reader is referred to the web version of this article.)

Table 1
Unit cell parameters, BET surface area and band gap values for as-prepared $Bi_3Ti_{1-2x}Cr_xNb_{1+x}O_9$ (x = 0, 0.1, 0.2).

Sample	Space group	a/Å	b/Å	c/Å	V/Å³	BET suface area/(m²/g)	Band gap/eV
Bi_3TiNbO_9	$A2_1am$	5.4361(3)	5.4028(3)	25.102(2)	737.25(9)	2.05(1)	3.17(4)
x = 0.1	$A2_1am$	5.4401(3)	5.4071(3)	25.112(2)	738.69(7)	1.78(1)	2.27(1)
x = 0.2	$A2_1am$	5.4477(3)	5.4207(3)	25.143(2)	742.48(8)	4.87(1)	2.15(1)
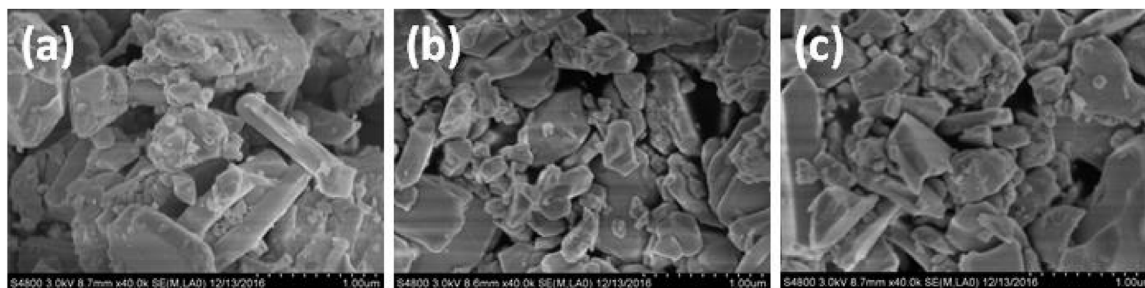
Fig. 3. Field emission scanning electron microscopy images of $Bi_3Ti_{1-2x}Cr_xNb_{1+x}O_9$ (x = 0, 0.1, 0.2): (a) x = 0, (b) x = 0.1 and (c) x = 0.2.

torted $Bi(Ti, Nb, Cr)_2O_7$ perovskite slabs interleaved by Bi_2O_2 layers, as shown in the inserted image of Fig. 2. The limited Cr/Nb doping level could be originated from the mismatch between perovskite slab and Bi_2O_2 layer as doping severely expands the perovskite structure therefore breaks the bonding between Bi $6s^2$ lone pair in Bi_2O_2 layer and apical oxygens in the perovskite slab [56]. Nevertheless, we have successfully prepared Cr/Nb co-doped Bi_3TiNbO_9 with doping level up to 20%.

3.2. Microstructures

Microstructures of these samples were then inspected using field emission scanning electron microscopy (SEM) and high resolution transmission electron microscopy (HRTEM). SEM images of all sample powders reveals bulky particles with particle size varying from several hundred nano-meters to a few microns. This observation is consistent with our preparation method that involves high temperature calcination. However, their layered crystal structures can still be envisaged from those plate-like particles in Fig. 3. Cr/Nb co-doping seems have no apparent impact on the morphology of Bi_3TiNbO_9 and BET surface area of all samples is close and lower than 5 m²/g. The particles of Cr/Nb co-doped Bi_3TiNbO_9 were further examined under HRTEM conditions. Fig. 4 illustrates the typical HRTEM images of $Bi_3Ti_{0.6}Cr_{0.2}Nb_{1.2}O_9$ (x = 0.2) along different zone axes. Clear lattice fringes with separation commensurate to d spacing of corresponding lattice planes can be seen, confirming the formation of single phase compound. For instance, (002) lattice fringes can be easily identified by the separation of neighboring fringes as large as 12.58 Å in Fig. 4c. Interestingly, the structure lamination of this compound is verified by the periodical occurrence of dark and light fringes in the image, in good agreement with the alternative stacking of Bi_2O_2 layers and perovskite slabs in the structure. A schematic representation of refined crystal structure of $Bi_3Ti_{0.6}Cr_{0.2}Nb_{1.2}O_9$ (x = 0.2) (projected from [110] direction) is displayed in Fig. 4d, which closely resembles the lattice fringe arrangement in Fig. 4c, i.e. every two closely lied dark fringes separated by two light fringes. Therefore, the dark fringes correspond to the Bi_2O_2 layers and light ones to perovskite slabs. Similar phenomenon has been seen in other layered compounds [22].

3.3. UV–vis spectroscopy

Previous conductivity measurement suggests that pristine Bi_3TiNbO_9 has a band gap value of 3.4 ± 0.2 eV [57] and UV–vis spectroscopy analysis reported also confirms its negligible visi-

ble light absorption, although the band gap value is reported to 3.1 eV [36]. In our case, the as-synthesized Bi_3TiNbO_9 exhibits a pale yellow color but is tuned into dark yellow color after co-doped with Cr/Nb (Fig. 5b inserted image). The strong color after doping implies substantial visible light absorption. This is verified by their UV–vis absorption spectra. Pristine Bi_3TiNbO_9 demonstrates a sharp absorption edge around 400 nm and a small absorption tail extending to 450 nm. The small absorption tail thereby contributes to the pale yellow appearance of sample powders and Bi_3TiNbO_9 is essentially a wide band gap semiconductor. However, considerable visible light absorption can be observed in Cr/Nb co-doped samples. Their absorption curve in the visible light region is characterized by several absorption bands centered around 450 nm, 550 nm and 650 nm. Comparable to a number of Cr doped semiconductors, the band around 450 nm has been frequently assigned to metal to metal charge transfer (MMCT) either from $Cr^{3+} \rightarrow Ti^{4+}$ ($Cr^{3+} + Ti^{4+} \rightarrow Cr^{4+} + Ti^{3+}$) or from $Cr^{3+} \rightarrow Nb^{5+}$ ($Cr^{3+} + Nb^{5+} \rightarrow Cr^{4+} + Nb^{4+}$) [20,45,58–62]. The other two bands are probably due to d-d transitions of Cr^{3+} in octahedral crystal field. Thereby the band gap values of Cr/Nb co-doped Bi_3TiNbO_9 can be determined from the Kubelka-Munk transformation of absorption data by extrapolating the linear region down to x-axis. The Calculated band gap values are tabulated in Table 1. Apparently, Cr/Nb co-doping significantly reduces the band gap value of Bi_3TiNbO_9 by almost 1 eV.

3.4. X-ray photoelectron spectroscopy (XPS)

Information about the surface conditions is crucial to understand the catalytic properties of a photocatalyst. Binding energy of core-level electrons for constituent elements of Cr/Nb co-doped Bi_3TiNbO_9 is illustrated in Fig. 6. All data were adjusted according to the reference C 1s peak at 284.7 eV from adventitious carbon. The Bi 4f signals contains two sets of peaks due to spin-orbital splitting, which can be unfolded into four peaks. The peaks at high energy side at around 159.5 eV and 164.5 eV belongs to Bi $4f_{7/2}$ and Bi $4f_{5/2}$ states of Bi^{3+} species, respectively [63]. The presence of much stronger peaks at lower energy side (157.7 eV and 163.0 eV) implies the existence of a large portion of Bi species at low oxidation state, such as Bi^{2+} [64,65]. This is probably due to oxygen deficiency at sample surface [66,67] or the presence of impurity like BiO [65]. The XPS spectra for dopants Cr and Nb 3d signals are displayed in Fig. 6b and 6c. The Cr 3d signals involve two weak peaks at around 576 eV and 585.5 eV, assignable to $3d_{3/2}$ and $3d_{5/2}$ states of Cr^{3+} species [59,60]. The Nb 3d signals compose two over-
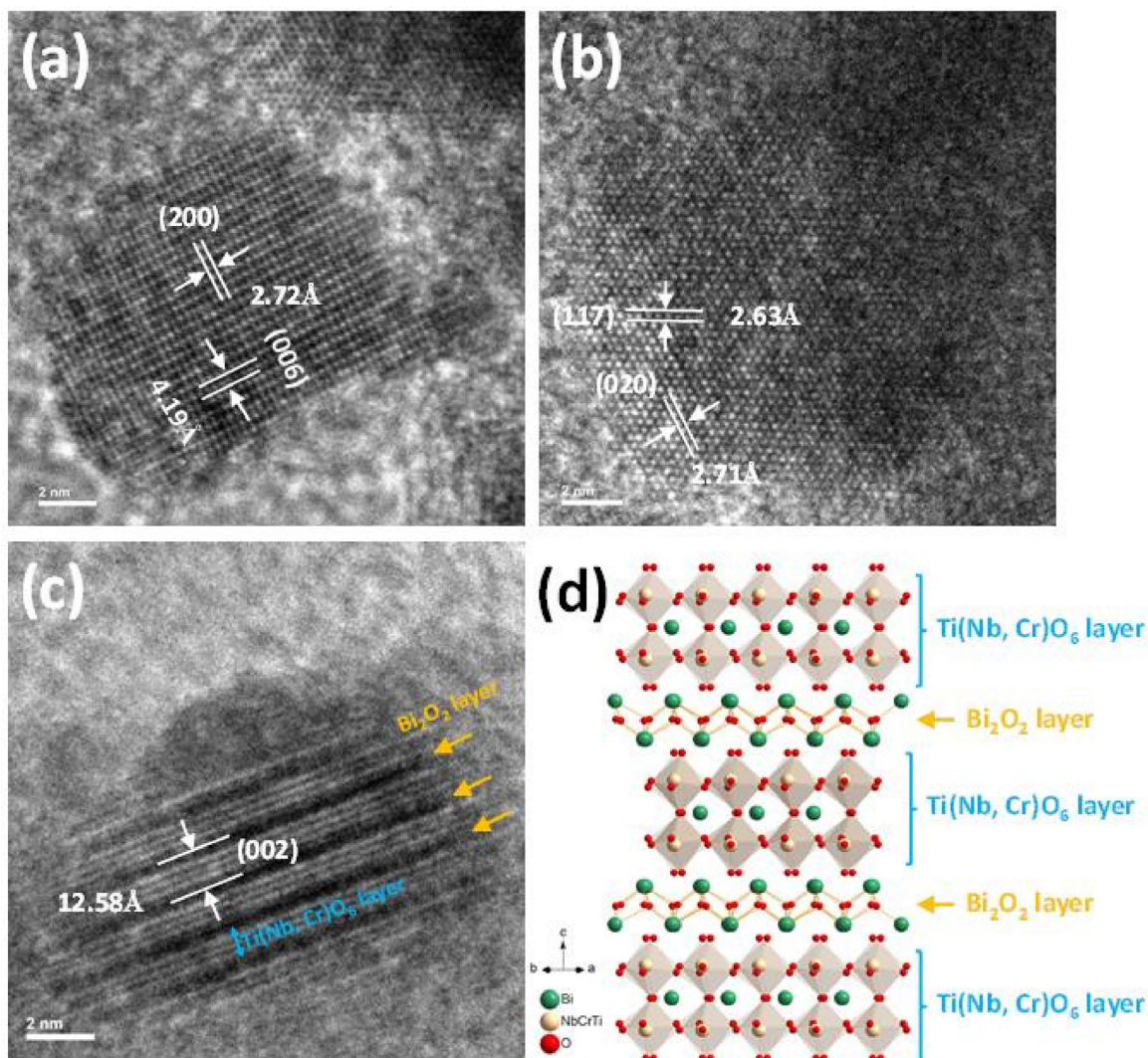
**Fig. 4.** High resolution transmission electron microscopy images of $Bi_3Ti_{0.6}Cr_{0.2}Nb_{1.2}O_9$ (x = 0.2): (a) along {010} zone axis, (b) along {70-1} zone axis, (c) showing the (002) lattice fringe and (d) a refined crystal structure projected from [110] direction.

lapping peaks at around 207 eV and 210 eV, corresponding to $3d_{3/2}$ and $3d_{5/2}$ states of Nb^{5+} species [68]. The O 1s signals, however, contains several broad peaks centered at around 529 eV, 531 eV and 533 eV, attributable to lattice oxygen, surface OH groups and carbonate species [45]. It is clear that peak for surface OH group dominates the O 1s signals, suggesting that the surface of all these Aurivillius compounds are highly hydrophilic. The Ti 2p signals are severely masked by Bi $4d_{3/2}$ peaks but can be roughly identified to Ti^{4+} species [63] (Fig. S1).

3.5. Photocatalytic hydrogen production and PEC analysis

The photocatalytic properties of these samples were then evaluated by monitoring the hydrogen production from water in the presence of sacrificial agent under different irradiation conditions. 1 wt% Pt was used as a cocatalyst to promote photo-reduction reactions. Control experiments with either sample powders or light illumination missing did not give rise to hydrogen evolution, confirming the absence of spontaneous hydrogen evolution reactions. Immediate hydrogen signals were detected as soon as sample powders were subjected to full range illumination ($\lambda \geq 250$ nm), indicating a real photocatalytic process. Fig. 7a illustrates the temporal hydrogen evolution of all samples under full range illu-

mination. Continuous hydrogen production was seen during the whole experimental timeframe, suggesting that they are efficient photocatalysts for photo-reduction reactions. Interestingly, both Cr/Nb co-doped samples exhibit a much higher activity than pristine Bi_3TiNbO_9, highlighting the benefit of doping. The highest activity belongs to $Bi_3Ti_{0.8}Cr_{0.1}Nb_{1.1}O_9$ (x = 0.1) which produces more than twice as much hydrogen as pristine Bi_3TiNbO_9 for 2.5 h. Nevertheless, further increasing Cr/Nb doping level leads to appreciable decrease in photocatalytic activity by almost 40%, indicating that some negative effects of doping starts to dominate at high doping levels. It is known that deep levels formed by Cr are well known recombination centers as compared to shallow levels, contributing to the decreased activity at high doping levels. Previous investigations have confirmed that the dopants could also serve as additional charge recombination centers thereby severely decrease the activity [69]. However, this is not the case under visible light illumination ($\lambda \geq 420$ nm) as hydrogen evolution strongly correlates to the doping levels albeit the photocatalytic activity is much lower than those under full range illumination. The experiment for $Bi_3Ti_{0.8}Cr_{0.1}Nb_{1.1}O_9$ (x = 0.1) has been extended to another two cycles to examine the stability of the sample (Fig. S2). A clear increase in photocatalytic hydrogen production can be noticed in the second and third cycle, probably due to the surface activa-
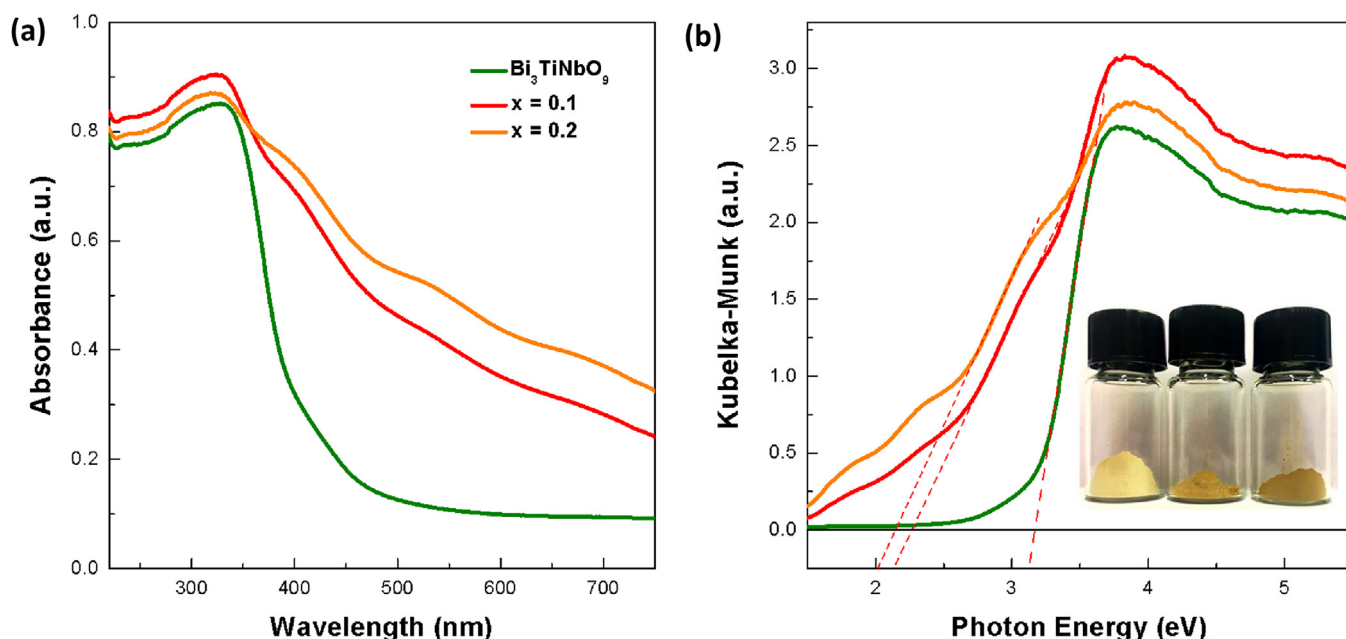
Fig. 5. (a) UV–vis light absorption spectra (converted from diffuse reflectance spectra) of freshly prepared samples and (b) Kubelka-Munk transformation of diffuse reflectance data, a digital photograph of sample powders is inserted for visual inspections.

tion phenomenon where surface defects is suppressed and reaction site is enhanced. Interestingly, the sample shows a better activity than commercial P25 in the third cycle even though P25 has a much larger surface area than the sample studied in this work ($\sim$50 m^2/g vs $\sim$2 m^2/g) (Fig. S4). Besides, XRD analysis before and after photocatalytic experiment suggests no discernable changes, confirming the stability of the sample (Fig. S3). The average photocatalytic hydrogen production rate under different irradiation conditions are summarized in Fig. 7b. $Bi_3Ti_{0.8}Cr_{0.1}Nb_{1.1}O_9$ (x = 0.1) gives the highest average hydrogen production rate under full range illumination $\sim$41.11 μmol/h, corresponding to AQE $\sim$0.52% and $Bi_3Ti_{0.6}Cr_{0.2}Nb_{1.2}O_9$ (x = 0.2) demonstrates the highest average hydrogen production rate under visible light illumination $\sim$9.21 μmol/h with AQE $\sim$0.27%. These values are better than or at least comparable to a number of photocatalysts [20,41,70]. It is worth mentioning that the AQE gives the lowest estimate of the real quantum efficiency since long wavelength photons and photons scattered/reflected by sample powders and electrolyte are all included during calculation. The AQE for a particular wavelength λ = 420 nm is also calculated by considering the hydrogen produced under 420 nm photon illumination. About 3.56 μmol/h H$_2$ was generated for $Bi_3Ti_{0.6}Cr_{0.2}Nb_{1.2}O_9$ (x = 0.2) under 420 nm photon illumination (photon flux 228.56 μmol/m^2/s), approaching AQE $\sim$0.31% at 420 nm. The effect of Cr/Nb co-doping can be understood by comparing the activity of Cr doped sample under the same conditions (Fig. S5). Cr doped Bi_3TiNbO_9 (nominal composition $Bi_3Ti_{0.9}Cr_{0.1}NbO_{9-\delta}$) generally contains impurity phase $Bi_4Ti_3O_{12}$ and exhibits a much poorer activity than Cr/Nb co-doped Bi_3TiNbO_9 ($Bi_3Ti_{0.8}Cr_{0.1}Nb_{1.1}O_9$ (x = 0.1)). Thereby dopant Nb contributes to the single phase formation (by charge compensation) and has positive effects on the photocatalytic activity. The benefits of Cr/Nb co-doping are also verified by photoelectrochemical (PEC) analysis as seen in Fig. 8. Linear sweep voltammetry (LSV) measurements under chopped light illumination reveal a much higher anodic photocurrent for both visible light ($\lambda \geq$ 420 nm) and AM 1.5 conditions, highlighting the positive effects of introducing Cr/Nb into Bi_3TiNbO_9. These results are consistent with photocatalytic properties that significant enhancement in hydrogen production rate is observed in Cr/Nb co-doped samples. It is interesting to see a small

anodic peak around 0.2 V (vs. NHE) which might be related to the oxidation of Bi species at low oxidation states.

3.6. Theoretical calculations

For better understanding the dissimilar trend of photocatalytic activity under different irradiation conditions, we carried out theoretical calculations on the electronic structures before and after Cr/Nb co-doping. The calculations were based on pristine Bi_3TiNbO_9 unit cell and doping was considered by randomly substituting 2 Ti atoms with 1 Cr and 1 Nb atom. The calculated results are illustrated in Fig. 9. Bi_3TiNbO_9 is an indirect band gap semiconductor with a calculated indirect band gap value $\sim$2.36 eV and direct band gap value $\sim$2.49 eV. These values are about 0.7 eV smaller than the experimental one $\sim$3.1 eV from UV–vis absorption spectrum. This discrepancy can be attributed to the drawbacks of the generalized gradient approximation (GGA) method that often underestimates the band gaps [71]. Nevertheless, the indirect nature of pristine Bi_3TiNbO_9 well explains the absorption tail observed in its UV–vis spectrum and poor photocatalytic activity under visible light illumination [72]. DOS and PDOS analysis suggests that the bottom of conduction band (CB) constitutes mainly Ti 3d and Nb 4d orbitals while the top of valence band (VB) is of O 2p and Bi 6s characters. The involvement of Bi 6s electrons at the top of VB is probably responsible for the indirect nature of Bi_3TiNbO_9. On the contrary, the Cr/Nb co-doping introduces an additional spin polarized valence band (SPVB) in the original band gap of Bi_3TiNbO_9, being the reason for a small band gap and visible light absorption. The SPVB owns dominantly Cr 3d character and is frequently seen in a number of Cr doped wide band gap semiconductors [20,45,58,60]. The indirect nature of Bi_3TiNbO_9 is maintained after doping, so does the top of CB. The visible light absorption and corresponding visible light photocatalytic activity thus stems from the electron excitations from Cr 3d orbitals to Ti 3d and Nb 4d orbitals, i.e. $Cr^{3+} \rightarrow Ti^{4+}$ ($Cr^{3+} + Ti^{4+} \rightarrow Cr^{4+} + Ti^{3+}$) and $Cr^{3+} \rightarrow Nb^{5+}$ ($Cr^{3+} + Nb^{5+} \rightarrow Cr^{4+} + Nb^{4+}$), being consistent with previous spectroscopic analysis. In light of these results, we can now tentatively explain the different trends in photocatalytic activities under full range and visible light illumination. Under full range
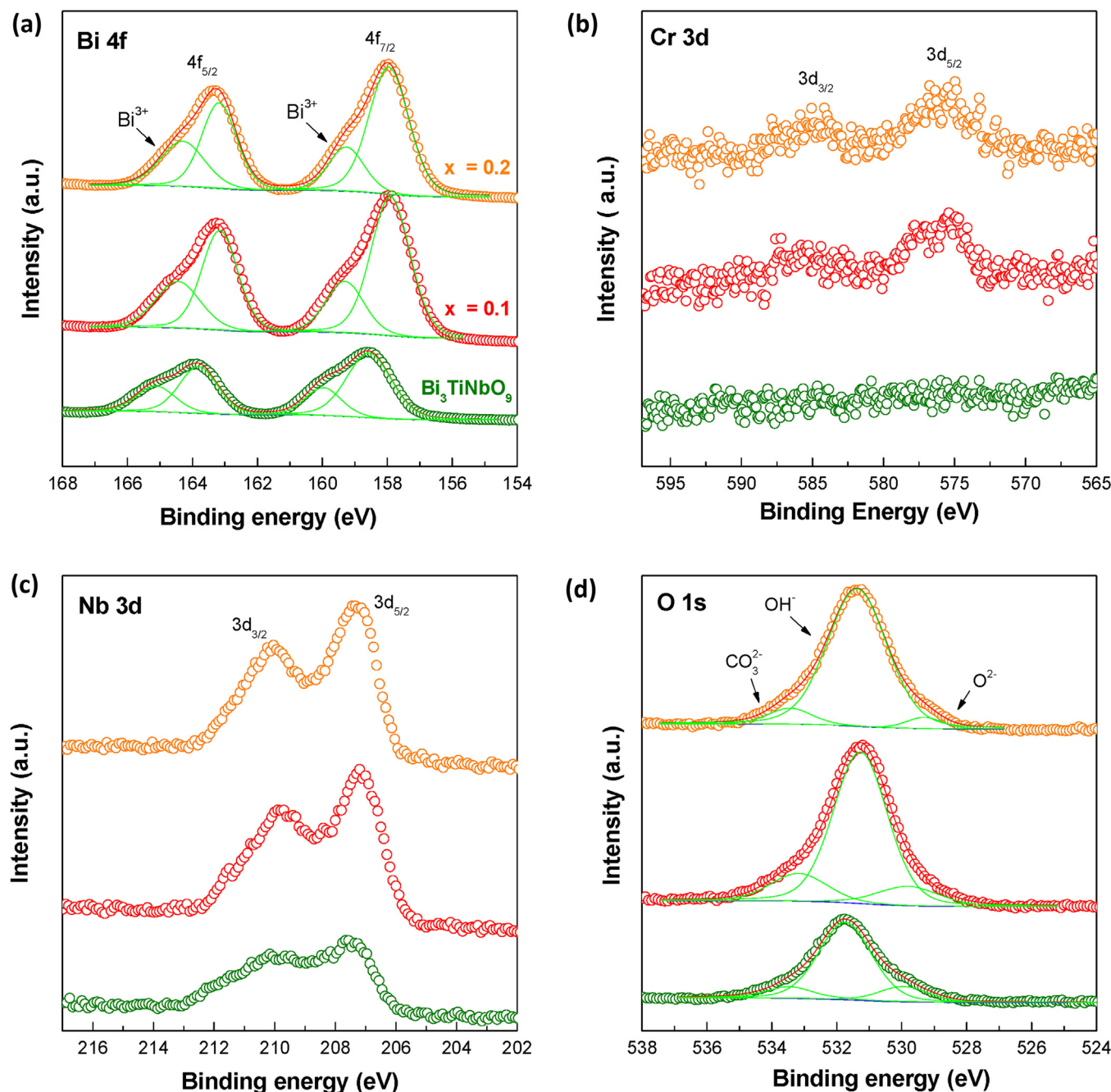
Fig. 6. X-ray photoelectron spectra (XPS) of samples: (a) Bi 4f peaks, (b) Cr 3d peaks, (c) Nb 3d peaks and (d) O 1s peaks.

illumination ($\lambda \geq 250$ nm), electron excitations from O $2p$ and Bi $6s$ orbitals to CB contributes to the major part of photocatalytic activity as holes formed in these orbitals have a high mobility. Introducing two much dopants would therefore decrease the activity as charge recombination events occur more easily in the presence of these dopants. Thereby, an optimal doping level exists albeit doping helps to extend light absorption. However, under visible light illumination, electron excitations occur exclusively between Cr and Ti/Nb, therefore a high level of Cr favors a high photocatalytic activity. More importantly, close examination of their band structures suggest anisotropic charge transportation features. For instance, band dispersion from **S** to **R** governs the electron behavior along [001] direction where nearly flat curves are seen with zero dispersion in energy. The effective mass of both electrons and holes in

this direction is expected to be enormously high thereby essentially prohibits practical transportations along this direction [73]. Such peculiar band dispersion is not seen in other directions such as [100] (from **Γ** to **Y**) and [010] (From **Y** to **S**), revealing that Bi_3TiNbO_9 has 2D charge transportation properties. Further analysis of decomposed charge density at conduction band minimum (CBM) and valence band maximum (VBM) suggests that CBM and VBM are dominantly located within perovskite slabs (Fig. 10). More specifically, CBM consists of Ti $3d$ and Nb $4d$ orbitals which is exclusively buried in $[BiTiNbO_7]^{2-}$ perovskite slabs while VBM is composed by the hybridization of O $2p$ and Bi $6s$ orbitals predominantly from $[BiTiNbO_7]^{2-}$ perovskite slabs. The negligible contribution of $(Bi_2O_2)^{2+}$ fluorite-like layers to both CBM and VBM confirms 2D charge transportation properties of Bi_3TiNbO_9, i.e. electrons
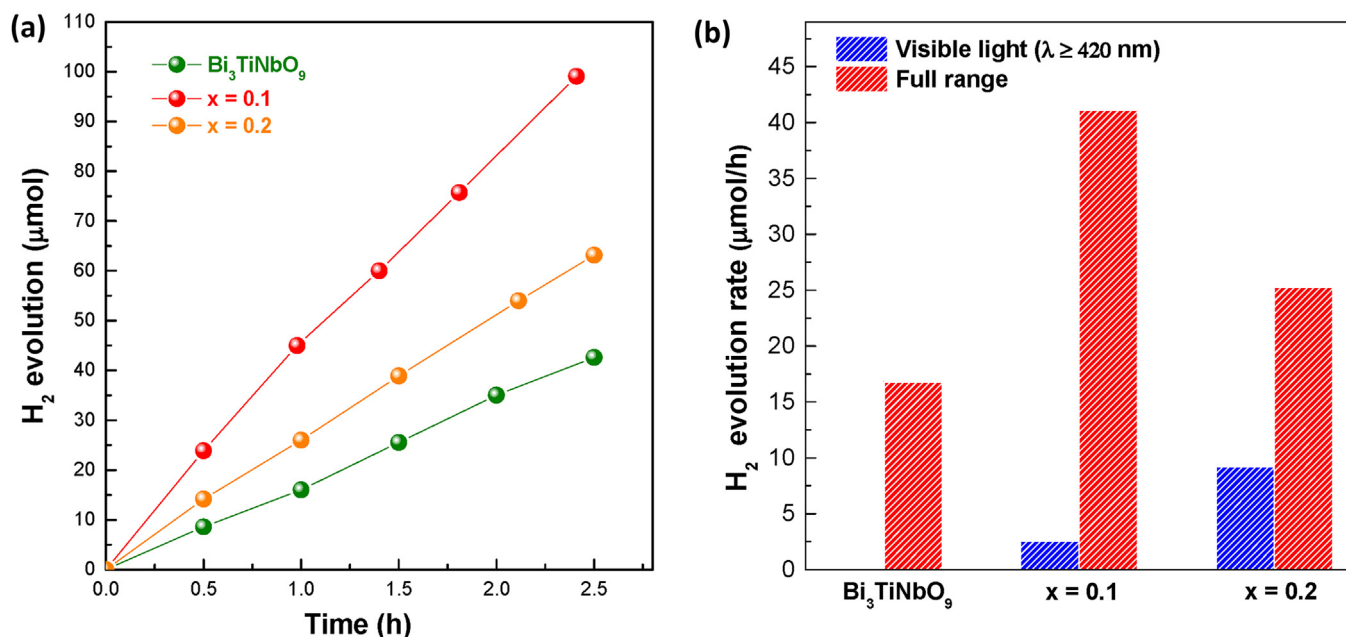
Fig. 7. (a) photocatalytic hydrogen production of all samples under full range illumination ($\lambda \geq 250$ nm) in sodium sulfite aqueous solution (0.05 M) and (b) average photocatalytic hydrogen production rate under full range ($\lambda \geq 250$ nm) and visible light illumination ($\lambda \geq 420$ nm).
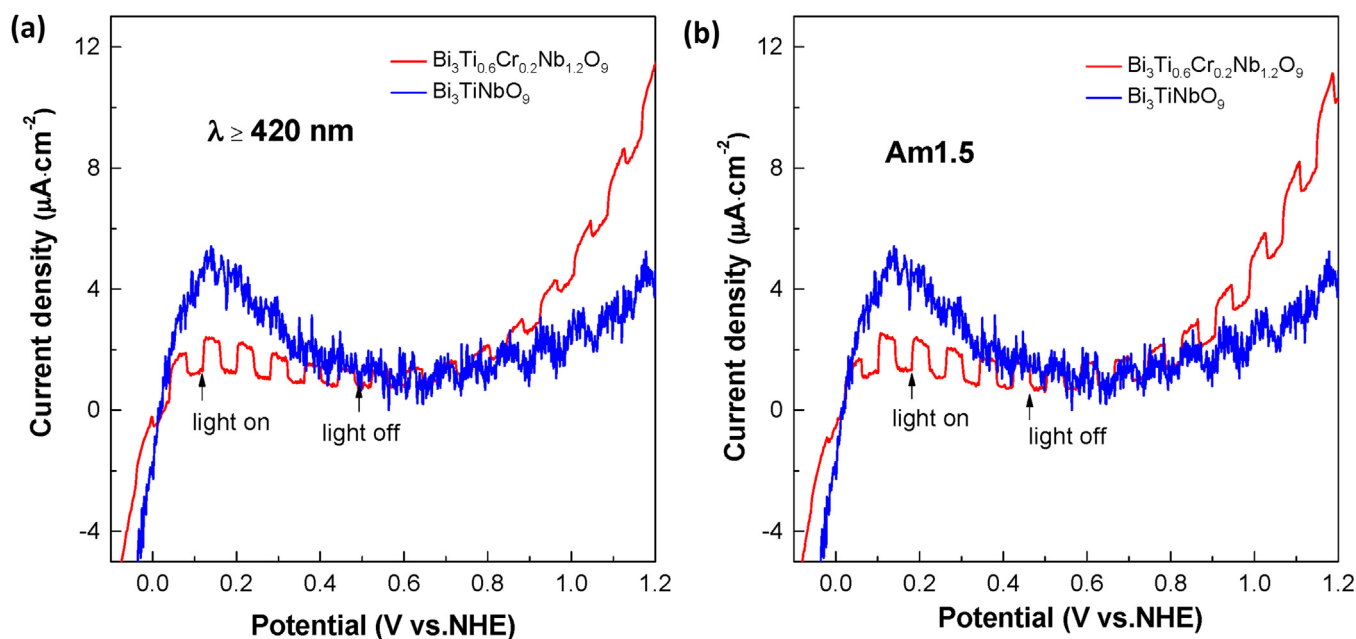

Fig. 8. Linear sweep voltammetry (LSV) of photoelectrodes fabricated from sample Bi_3TiNbO_9 and $Bi_3Ti_{0.6}Cr_{0.2}Nb_{1.2}O_9$ ($x = 0.2$) powders under chopped light illumination: (a) visible light ($\lambda \geq 420$ nm) and (b) AM 1.5.

and holes are only allowed to migrate within $[BiTiNbO_7]^{2-}$ perovskite slabs and transportation across $(Bi_2O_2)^{2+}$ fluorite-like layers is practically forbidden. This is extremely helpful for photocatalytic performance as interlayer charge recombination can be effectively suppressed. Previous analysis on the ferroelectricity of Bi_3TiNbO_9 suggested that its ferroelectricity stems mainly from the a-axis displacement of Bi atoms in the $[BiTiNbO_7]^{2-}$ perovskite slabs instead of Ti(Nb) off-centering in the octahedrons [74]. In other words, the $Ti(Nb)O_6$ octahedral networks can be held almost intact during ferroelectric poling which guarantees rapid electron-hole separations. All these analysis suggests that Bi_3TiNbO_9 is a promising ferroelectric compound for photocatalytic reactions.

4. Conclusions

We have successfully prepared Bi_3TiNbO_9 and its Cr/Nb co-doped counterparts via solid state reactions. The crystal structure of Bi_3TiNbO_9 is maintained after Cr/Nb doping with a slight expansion in unit cell. The solubility limit of Cr/Nb dopants in the Bi_3TiNbO_9 crystal lattice lies around 20%. Pristine Bi_3TiNbO_9 is essentially a wide band semiconductor with band gap around 3.1 eV. Co-doping Cr/Nb effectively reduces its band gap by almost 1 eV and extends its light absorption into visible light region. All doped Cr remains its low oxidation state (Cr^{3+}) and likely due to the presence of Nb which helps to build a charge-balanced system. The photocatalytic performance of Bi_3TiNbO_9 is greatly enhanced after doping Cr/Nb.
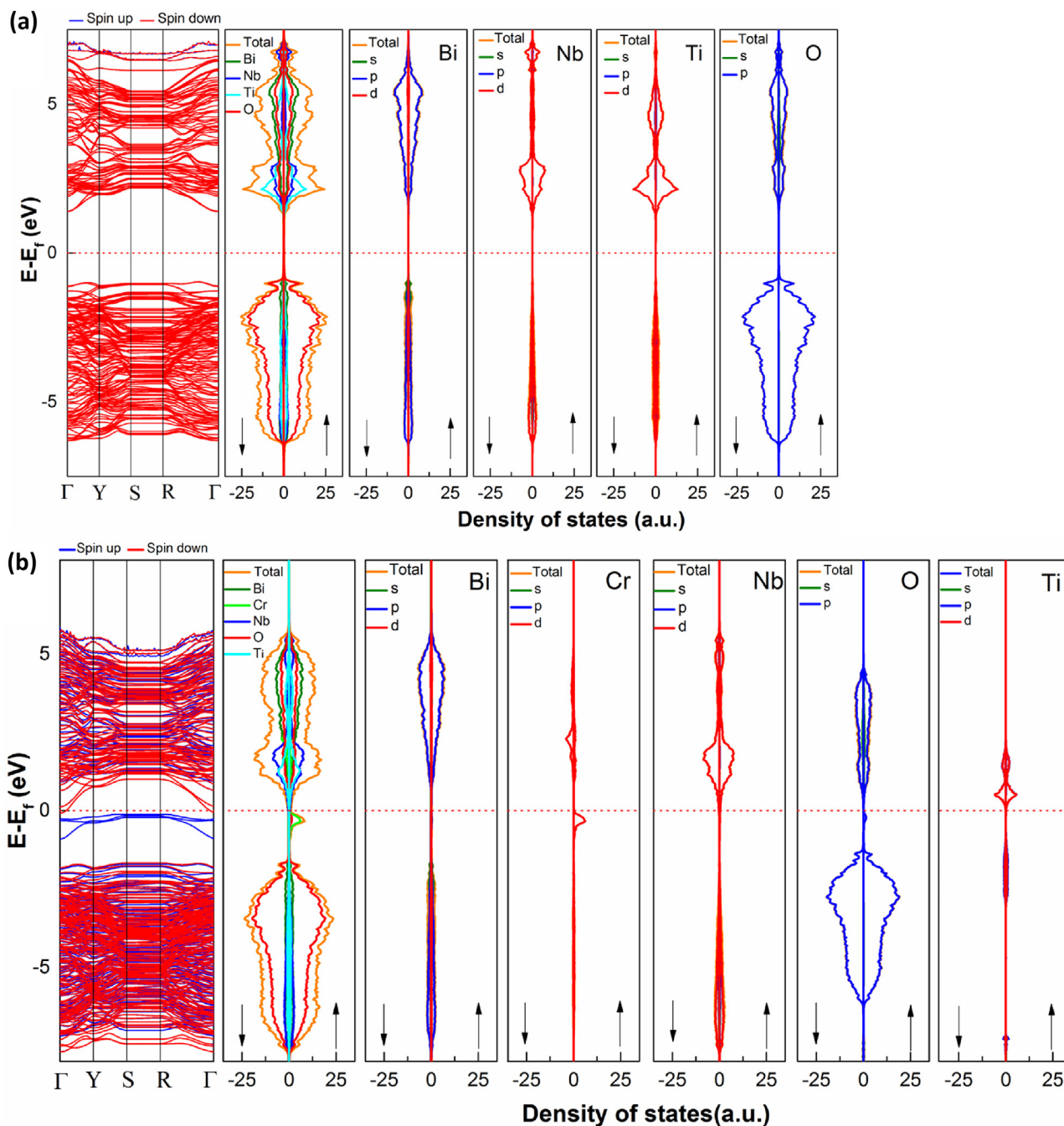
Fig. 9. Calculated band structures, total density of states (DOS) and projected density of states (PDOS) of constituent elements of (a) pristine Bi_3TiNbO_9 and (b) Cr/Nb co-doped Bi_3TiNbO_9.

$Bi_3Ti_{0.8}Cr_{0.1}Nb_{1.1}O_9$ (x = 0.1) gives the highest average hydrogen production rate under full range illumination ~41.11 μmol/h, corresponding to AQE ~0.52% and $Bi_3Ti_{0.6}Cr_{0.2}Nb_{1.2}O_9$ (x = 0.2) demonstrates the highest average hydrogen production rate under visible light illumination ~9.21 μmol/h with AQE ~0.27%. The superior photocatalytic activity is also verified by the higher anodic photocurrent in Cr/Nb co-doped Bi_3TiNbO_9. DFT calculation reveals the role of dopant Cr in forming a new valence band inside the original band gap of Bi_3TiNbO_9 thereby is responsible for the band gap reduction and visible light photocatalytic activity. The dissimilar trend of photocatalytic hydrogen production with regard to Cr/Nb doping levels under visible light and full range illumination is probably stems from the different photon excitation processes that involves in the photocatalytic reactions. More importantly, DFT calculation suggests that Bi_3TiNbO_9 has anisotropic charge transportation properties, with electrons and holes exclusively migration within $[BiTiNbO_7]^{2-}$ perovskite slabs.
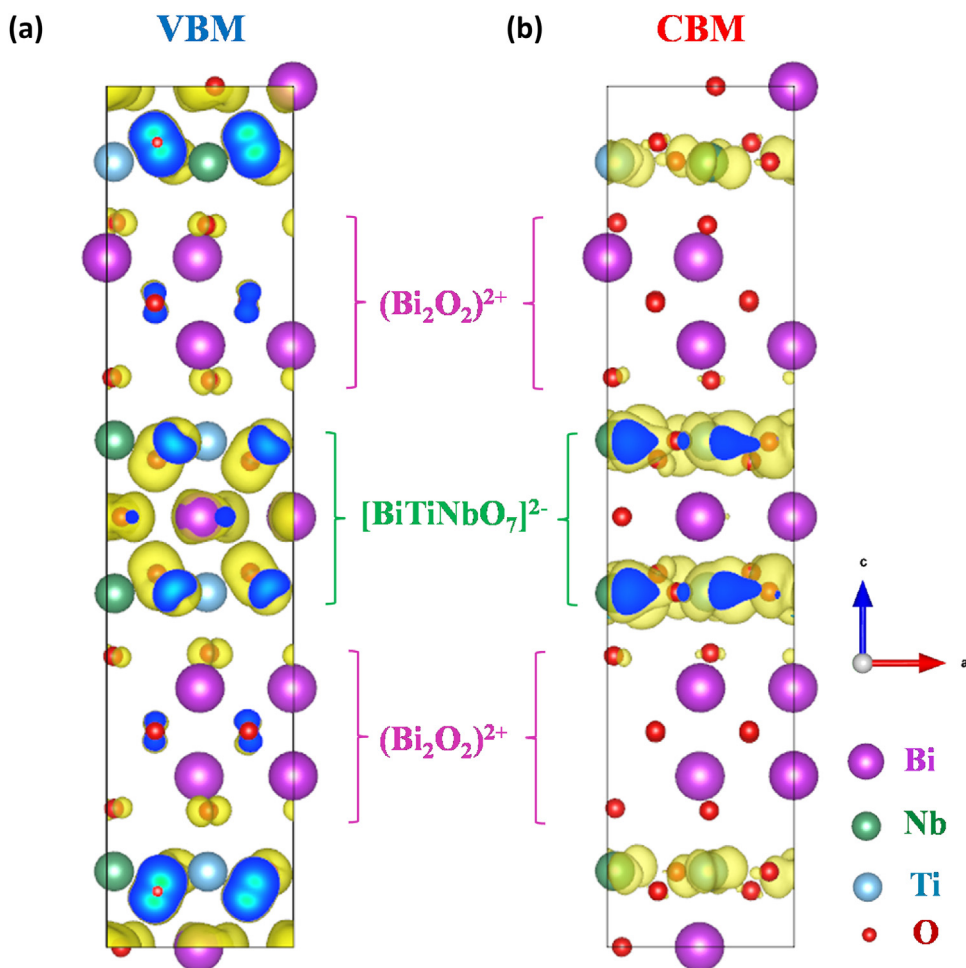
Fig. 10. Decomposed charge density of Bi_3TiNbO_9 at VBM (a) and CBM (b), unit cell is marked by black lines.

Appendix A. Supplementary data

Supplementary data associated with this article can be found, in the online version, at http://dx.doi.org/10.1016/j.apcatb.2017.06.012.

References

[1] Annual Energy Outlook, 2014, U.S. Energy Information Administration, 2014.
[2] B. Dudley, BP Statistical Review of World Energy (June 2014), 2014.
[3] N.S. Lewis, D.G. Nocera, Proc. Natl. Acad. Sci. U. S. A. 103 (2006) 15729–15735.
[4] D.G. Nocera, Chem. Soc. Rev. 38 (2009) 13–15.
[5] Z.G. Zou, J.H. Ye, K. Sayama, H. Arakawa, Nature 414 (2001) 625–627.
[6] F.T. Wagner, G.A. Somorjai, Nature 285 (1980) 559–560.
[7] K. Maeda, K. Teramura, D.L. Lu, T. Takata, N. Saito, Y. Inoue, K. Domen, Nature 440 (2006) 295.
[8] A. Listorti, J. Durrant, J. Barber, Nat. Mater. 8 (2009) 929–930.
[9] X.X. Xu, C. Randorn, P. Efstathiou, J.T.S. Irvine, Nat. Mater. 11 (2012) 595–598.
[10] M.S. Zhu, X.Y. Cai, M. Fujitsuka, J.Y. Zhang, T. Majima, Angew. Chem. Int. Ed. 56 (2017) 2064–2068.
[11] Z.K. Yue, A.J. Liu, C.Y. Zhang, J. Huang, M.S. Zhu, Y.K. Du, P. Yang, Appl. Catal. B: Environ. 201 (2017) 202–210.
[12] Y.J. Wu, Z.K. Yue, A.J. Liu, P. Yang, M.S. Zhu, ACS Sustainable Chem. Eng. 4 (2016) 2569–2577.
[13] K. Sivula, R. van de Krol, Nat. Rev. Mater. 1 (2016).
[14] J.R. Bolton, S.J. Strickler, J.S. Connolly, Nature 316 (1985) 495–500.
[15] Z.B. Chen, T.F. Jaramillo, T.G. Deutsch, A. Kleiman-Shwarstein, A.J. Forman, N. Gaillard, R. Garland, K. Takanabe, C. Heske, M. Sunkara, E.W. McFarland, K. Domen, E.L. Miller, J.A. Turner, H.N. Dinh, J. Mater. Res. 25 (2010) 3–16.
[16] M.R. Hoffmann, S.T. Martin, W.Y. Choi, D.W. Bahnemann, Chem. Rev. 95 (1995) 69–96.
[17] A. Kudo, H. Kato, S. Nakagawa, J. Phys. Chem. B 104 (2000) 571–575.
[18] Y. Miseki, H. Kato, A. Kudo, Energ. Environ. Sci. 2 (2009) 306–314.
[19] S. Ikeda, M. Hara, J.N. Kondo, K. Domen, H. Takahashi, T. Okubo, M. Kakihana, J. Mater. Res. 13 (1998) 852–855.
[20] X.Q. Sun, Y.H. Xie, F.F. Wu, H.M. Chen, M.L. Lv, S. Ni, G. Liu, X.X. Xu, Inorg. Chem. 54 (2015) 7445–7453.
[21] X.Q. Sun, X.X. Xu, Appl. Catal. B: Environ. 210 (2017) 149–159.
[22] M.L. Lv, G. Liu, X.X. Xu, ACS Appl. Mater. Interfaces 8 (2016) 28700–28708.
[23] H.M. Chen, X.X. Xu, Appl. Catal. B: Environ. 206 (2017) 35–43.
[24] A. Etogo, R. Liu, J.B. Ren, L.W. Qi, C.C. Zheng, J.Q. Ning, Y.J. Zhong, Y. Hu, J. Mater. Chem. A 4 (2016) 13242–13250.
[25] Y.G. Zhou, Y.F. Zhang, M.S. Lin, J.L. Long, Z.Z. Zhang, H.X. Lin, J.C.S. Wu, X.X. Wang, Nat. Commun. 6 (2015).
[26] L.W. Zhang, Y.J. Wang, H.Y. Cheng, W.Q. Yao, Y.F. Zhu, Adv. Mater. 21 (2009), 1286-+.
[27] J.G. Hou, R. Cao, Z. Wang, S.Q. Jiao, H.M. Zhu, J. Mater. Chem. 21 (2011) 7296–7301.
[28] H.Q. He, J. Yin, Y.X. Li, Y. Zhang, H.S. Qiu, J.B. Xu, T. Xu, C.Y. Wang, Appl. Catal. B: Environ. 156 (2014) 35–43.
[29] H.J. Zhang, G. Chen, X. Li, Solid State Ionics 180 (2009) 1599–1603.
[30] N.I. Medvedeva, V.A. Gubanov, J. Struct. Chem. 37 (1996) 409–416.
[31] Y. Kitanaka, S. Katayama, Y. Noguchi, M. Miyayama, Jpn. J. Appl. Phys. 46 (2007) 7028–7030.
[32] Z. Zhang, H.X. Yan, X.L. Dong, Y.L. Wang, Mater. Res. Bull. 38 (2003) 241–248.
[33] Z.Y. Zhou, X.L. Dong, H.X. Yan, H. Chen, C.L. Mao, J. Appl. Phys. 100 (2006).
[34] D. Su, J.S. Zhu, Q.Y. Xu, J.S. Liu, Y.N. Wang, Microelectron. Eng. 66 (2003) 825–829.
[35] Z.Y. Zhou, B.Z. Cheng, Y.C. Li, X.F. Dong, Mater. Chem. Phys. 104 (2007) 225–229.
[36] L. Xu, Y.P. Wan, H.D. Xie, Y.L. Huang, X.B. Qiao, L. Qin, H.J. Seo, J. Am. Ceram. Soc. 99 (2016) 3964–3972.
[37] H.M. Yin, A.Q. Zhou, N. Chang, X.H. Xu, Mater. Res. Bull. 44 (2009) 377–380.
[38] A.C. Larson, R.B. Von Dreele, Los Alamos National Laboratory Report No. LA-UR-86-748 (1994).
[39] G. Kortum, W. Braun, G. Herzog, Angew. Chem. Int. Ed. 2 (1963) 333–341.
[40] P.V.d. Heide, X-ray Photoelectron Spectroscopy—An Introduction to Principles and Practices, John Wiley & Sons, Inc, Hoboken, 2012.

[41] L.W. Lu, M.L. Lv, D. Wang, G. Liu, X.X. Xu, Appl. Catal. B: Environ. 200 (2017) 412–419.
[42] L.W. Lu, M.L. Lv, G. Liu, X.X. Xu, Appl. Surf. Sci. 391 (2017) 535–541.
[43] X.X. Xu, A.K. Azad, J.T.S. Irvine, Catal. Today 199 (2013) 22–26.
[44] X.X. Xu, G. Liu, C. Randorn, J.T.S. Irvine, Int. J. Hydrogen Energy 36 (2011) 13501–13507.
[45] X.X. Xu, Y.H. Xie, S. Ni, A.K. Azad, T.C. Cao, J. Solid State Chem. 230 (2015) 95–101.
[46] F.F. Wu, G. Liu, X.X. Xu, J. Catal. 346 (2017) 10–20.
[47] H.M. Chen, Y.H. Xie, X.Q. Sun, M.L. Lv, F.F. Wu, L. Zhang, L. Li, X.X. Xu, Dalton T. 44 (2015) 13030–13039.
[48] Y.H. Xie, Y.W. Wang, Z.F. Chen, X.X. Xu, ChemSusChem 9 (2016) 1403–1412.
[49] Y.W. Wang, D.Z. Zhu, X.X. Xu, ACS Appl. Mater. Interfaces 8 (2016) 35407–35418.
[50] G. Kresse, J. Furthmuller, Phys. Rev. B 54 (1996) 11169–11186.
[51] J.P. Perdew, K. Burke, M. Ernzerhof, Phys. Rev. Lett. 77 (1996) 3865–3868.
[52] G. Kresse, D. Joubert, Phys. Rev. B 59 (1999) 1758–1775.
[53] H.J. Monkhorst, J.D. Pack, Phys. Rev. B 13 (1976) 5188–5192.
[54] R.D. Shannon, C.T. Prewitt, Acta Crystallogr. B 25 (1969) 925–946.
[55] R.D. Shannon, C.T. Prewitt, Acta Crystall. B: Struct. 26 (1970) 1046–1048.
[56] R.H. Mitchell, Perovskites: Modern and Ancient, Almaz Press Inc., Ontario, Canada, 2002.
[57] H.X. Yan, H.T. Zhang, Z. Zhang, R. Ubic, M.J. Reece, J. Eur. Ceram. Soc. 26 (2006) 2785–2792.
[58] M.L. Lv, S. Ni, Z. Wang, T.C. Cao, X.X. Xu, Int. J. Hydrogen Energy 41 (2016) 1550–1558.
[59] X.X. Xu, M.L. Lv, X.Q. Sun, G. Liu, J. Mater. Sci. 51 (2016) 6464–6473.
[60] M.L. Lv, Y.H. Xie, Y.W. Wang, X.Q. Sun, F.F. Wu, H.M. Chen, S.W. Wang, C. Shen, Z.F. Chen, S. Ni, G. Liu, X.X. Xu, Phys. Chem. Chem. Phys. 17 (2015) 26320–26329.
[61] Y.S. Jia, S. Shen, D.G. Wang, X. Wang, J.Y. Shi, F.X. Zhang, H.X. Han, C. Li, J. Mater. Chem. A 1 (2013) 7905–7912.
[62] T. Ishii, H. Kato, A. Kudo, J. Photochem. Photobiol. A 163 (2004) 181–186.
[63] Y. Guo, J.H. Li, Z.Q. Gao, X. Zhu, Y. Liu, Z.B. Wei, W. Zhao, C. Sun, Appl. Catal. B: Environ. 192 (2016) 57–71.
[64] G.K. Zhang, J.L. Yang, S.M. Zhang, Q. Xiong, B.B. Huang, J.T. Wang, W.Q. Gong, J. Hazard. Mater. 172 (2009) 986–992.
[65] A. Gulino, S. LaDelfa, I. Fragala, R.G. Egdell, Chem. Mater. 8 (1996) 1287–1291.
[66] L.Y. Ding, R.J. Wei, H. Chen, J.C. Hu, J.L. Li, Appl. Catal. B: Environ. 172 (2015) 91–99.
[67] Q.Q. Wang, L.P. Yuan, M. Dun, X.M. Yang, H. Chen, J.L. Li, J.C. Hu, Appl. Catal. B: Environ. 196 (2016) 127–134.
[68] F.F. Wu, M.L. Lv, X.Q. Sun, Y.H. Xie, H.M. Chen, S. Ni, G. Liu, X.X. Xu, ChemCatChem 8 (2016) 615–623.
[69] H. Irie, Y. Watanabe, K. Hashimoto, J. Phys. Chem. B 107 (2003) 5483–5486.
[70] X.Q. Sun, S.W. Wang, C. Shen, X.X. Xu, ChemCatChem 8 (2016) 2289–2295.
[71] H. Xiao, J. Tahir-Kheli, W.A. Goddard, J. Phys. Chem. Lett. 2 (2011) 212–217.
[72] C. Kittel, Introduction to Solid State Physics, 8th ed., Wiley Hoboken, NJ, 2005.
[73] C. Kittel, Introduction to Solid State Physics, Wiley, New York, 1953.
[74] R.L. Withers, J.G. Thompson, A.D. Rae, J. Solid State Chem. 94 (1991) 404–417.